


 Cite this: *RSC Adv.*, 2026, 16, 6915

Corrosion inhibition of mild steel using eco-friendly porous nanocarbon derived from waste mango kernels: a step towards sustainability

 Anvitha Murari,^a Arathi A,^b Uraiwan Sirimahachai,^c Srilatha Rao^b and Gurumurthy Hegde^{*a}

The pervasive corrosion of mild steel in acidic media poses a significant challenge in various industrial applications. While existing synthetic corrosion inhibitors are effective, their high cost and environmental toxicity necessitate the development of more sustainable alternatives. In this study, we present a novel approach to corrosion mitigation employing a porous nanocarbon synthesized from mango kernels, a sustainable source of agricultural waste. The CNS inhibitor was synthesized *via* pyrolysis at 800 °C, yielding a high surface area (1090.2 m² g⁻¹) as confirmed by BET analysis. FE-SEM revealed a well-developed spherical morphology with an average particle size of 60–70 nm. The corrosion inhibition efficiency of CNS was evaluated for mild steel in 1 M HCl using a combination of electrochemical techniques, including open circuit potential, potentiodynamic polarization (PDP), and electrochemical impedance spectroscopy. The CNS derived from waste mango kernels, exhibited excellent inhibition performance, achieving an efficiency of up to 87.1% at 800 ppm. PDP results revealed a mixed-type inhibition mechanism with suppression in both anodic and cathodic reactions. The thermodynamic parameter, adsorption free energy ($\Delta G_{\text{ads}}^{\circ}$) of about -20.0 kJ mol⁻¹, indicates a spontaneous process and predominantly physical adsorption. Adsorption behavior was consistent with the Langmuir isotherm model. Surface analyses using SEM, EDS, optical profilometry, and water contact angle measurements corroborated the formation of a protective inhibitor film on the steel surface. These findings highlight the potential of bio-waste-derived materials as a sustainable and environmentally benign corrosion inhibitor for mild steel in acidic environments.

 Received 16th December 2025
 Accepted 26th January 2026

DOI: 10.1039/d5ra09725h

rsc.li/rsc-advances

1 Introduction

Mild steel (MS) remains a vital material for industrial infrastructure due to its strength, ductility, and low cost. However, its performance in acidic environments is often compromised due to rapid corrosion, particularly in hydrochloric acid (HCl) medium, which is widely used in pickling, oil well acidizing, and descaling processes.¹ Despite being an indispensable industrial process for removing rust and oxides, the use of strong acids in acid pickling and cleaning results in severe corrosion of MS, which is why laboratory studies using corrosive media like 1 M HCl are essential for developing viable solutions to prevent metal degradation.^{2–4}

The high concentration of chloride ions in HCl medium promotes anodic iron dissolution and cathodic hydrogen

evolution, accelerating degradation and jeopardizing structural integrity.^{5,6} Notably, corrosion-induced failures have led to severe industrial disasters in recent years. Corrosion-related failures have been implicated in several catastrophic events worldwide. For instance, the rupture of the Sinopec and Donghuang II oil pipelines in Qingdao resulted in a devastating explosion that claimed 62 lives, injured 136 individuals, and caused an estimated economic loss exceeding USD 124.9 million. In another case, the Fukushima nuclear facility experienced leakage from a corroded storage tank, discharging nearly 300 metric tons of contaminated water into the ocean and forcing the suspension of fishing activities in the surrounding area.⁷ These incidents underscore the urgent need for effective corrosion mitigation strategies in aggressive environments.

Various strategies have been developed to mitigate the corrosion of MS, particularly in aggressive acidic environments. These include surface coatings, cathodic protection, alloying, and the use of corrosion inhibitors.^{8–10} Among these, corrosion inhibitors are one of the most widely employed methods due to their cost-effectiveness, ease of application, and efficiency in reducing metal dissolution. A wide range of chemical

^aDepartment of Chemistry, Christ University, Bengaluru, Karnataka-560029, India. E-mail: murthyhegde@gmail.com

^bDepartment of Chemistry, Nitte Meenakshi Institute of Technology, Nitte (Deemed to be University), Bengaluru, Karnataka-560064, India

^cCentre of Excellence for Innovation in Chemistry, Division of Physical Science, Faculty of Science, Prince of Songkla University, Hat Yai, Songkla 90112, Thailand



compounds has been explored as corrosion inhibitors, including organic and inorganic molecules, surfactants, polymers, ionic liquids, and liquid crystals.¹¹ These compounds typically function by adsorbing onto the metal surface to form a protective barrier that impedes both anodic and cathodic reactions.¹²

Conventional corrosion inhibitors, particularly organic molecules, are effective; however, many of these organic compounds are toxic, environmentally persistent, and non-biodegradable.¹³ On the otherhand, inorganic inhibitors such as chromates, phosphates, and silicates also present toxicity and long-term environmental concerns. Surfactant-based inhibitors, with their amphiphilic molecular structures, offer good adsorption behavior but their stability under high temperatures and extreme pH conditions remains limited, and their synthesis often involves non-renewable feedstocks and costly reagents.¹⁴

Plant-based inhibitors derived from extracts rich in alkaloids, flavonoids, and tannins, have demonstrated significant inhibition efficiency in acidic environments.¹⁵ Nonetheless, they suffer from inherent limitations such as batch-to-batch variability, the presence of multiple phytochemicals with synergistic or antagonistic effects, poor thermal stability, and challenges in isolating the active components.¹⁶

Recently, carbon-based nanomaterials have shown promising corrosion inhibition due to their high surface area, uniform shape, stability, tunable porosity and biocompatibility.¹⁷ Studies have confirmed the potential of graphene oxide, carbon nanotubes, and fullerene derivatives for corrosion inhibition in acidic settings.^{18,19} For instance, Jing *et al.* developed PANI tannate-modified carbon nanotubes that showed an inhibition efficiency of approximately 90% for MS in an HCl medium.²⁰ Similarly, Shirazi *et al.* utilized a copolymer poly(-aniline-co-*o*-anthranilic acid) with GO and MWCNT, achieving efficiencies of 83% and 89%, respectively, in an HCl medium.²¹ However, the high cost and complex synthesis methods of some of these carbon nanomaterials limit their industrial scalability, which has spurred interest in using biomass-derived carbon nanoparticles (CNP) as a low-cost, sustainable alternative.

Zhen *et al.*, for example, synthesized carbon dots (CDs) from natural chitosan, which yielded an impressive inhibition efficiency of about 97% for MS in an HCl medium.²² In another study, Kuriaya *et al.* synthesized CDs from garlic peels, showing an inhibition efficiency of approximately 79% over a two-hour period.²³ While these studies demonstrate the promise of carbon dots, there remains a significant gap in the literature regarding the use of biomass-derived porous nanocarbons for this application.

Biomass-derived CNP help in reducing the wastes from the environment, and can be transformed into high-purity carbon through pyrolysis.²⁴ Mango (*Mangifera indica*) is a widely cultivated tropical fruit, primarily processed for its edible pulp, leaving behind a substantial amount of seed waste, comprising 20–60% of the fruit's total weight. The kernel, which accounts for 45–75% of the seed mass, is typically discarded due to its limited commercial utility, contributing to an estimated 123 000 metric tonnes of global mango seed waste annually.^{25–27}

Composed primarily of cellulose (25.2%), hemicellulose (34.06%), and lignin (15.0%),²⁸ mango kernels possess a lignocellulosic structure well-suited for conversion into porous carbon materials. Given their abundance, renewable nature, and carbon-rich composition, mango kernels represent an attractive biomass source for sustainable materials development.

In this study, mango kernel waste was converted into porous carbon nanospheres (CNS) using a single-step, non-activated pyrolysis method under a nitrogen atmosphere. The resulting CNS exhibited a high specific surface area and was evaluated for its corrosion inhibition performance on MS in 1 M HCl solution. To the best of our knowledge, this is the first report employing mango kernel-derived porous carbon in corrosion protection.

The inhibition efficiency of the synthesized CNS was systematically assessed using potentiodynamic polarization (PDP), electrochemical impedance spectroscopy (EIS), adsorption isotherm modelling, surface morphology analysis (SEM-EDS and optical profilometry), and water contact angle (WCA) measurements. A comparative analysis was also performed across varying inhibitor concentrations (50–800 ppm) and temperatures (298–313 K) to understand the thermodynamic and kinetic parameters influencing the corrosion process. This study provides a sustainable pathway for utilizing mango waste while advancing the development of environmentally friendly carbon-based corrosion inhibitors.

2 Materials and methods

2.1 Synthesis of CNS

The waste mango kernels were collected and sun-dried for several days. The dried kernels were finely powdered using a mixer grinder and sieved with the help of a 75 μm sieve. The sieved sample was pyrolyzed using a quartz tube furnace at 800 °C with a ramp-up of 10° min^{-1} in an N₂ atmosphere with a flow rate of 0.5 L min^{-1} . In order to remove the silicate impurities, the pyrolyzed CNS was acid-washed (0.1 N HCl). Further, the CNS was washed with distilled water until it had a neutral pH. Detailed procedure is given in our previous work.²⁹ The CNS obtained was termed as MK800 and employed for further studies.

2.2 Structural and morphological characterization of CNS

The morphology and elemental distribution of the synthesized inhibitor were examined by field emission scanning electron microscopy (FESEM) and energy-dispersive X-ray spectroscopy (EDS) using an Apero system (Thermo Fisher Scientific, USA). The average particle size of the nanospheres was determined from FESEM images using ImageJ software. Transmission electron microscopy (TEM) was carried out on a Talos F200i instrument (Thermo Scientific, Czech Republic). X-ray photoelectron spectroscopy (XPS, ESCALAB 250Xi, Thermo Scientific) was employed to analyze elemental composition and chemical states. Brunauer–Emmett–Teller (BET) surface area, pore size, and pore volume were determined by N₂ adsorption–desorption



isotherms using a BELSORP-max system (Microtrac, Japan), and *t*-plot analysis. X-ray diffraction (XRD) patterns were recorded using a Miniflex 600 diffractometer (Rigaku, Japan) with Cu K α radiation. Raman spectra were acquired using a LabRAM HR system (Horiba, Renishaw) with a 532 nm excitation source.

2.3 Preparation of MS, acid medium, and inhibitor solution

MS specimens were prepared with an exposed surface area of 1 cm², while the remaining portions were insulated using an acrylic resin (DPI RR Cold Cure) coating. The metallic surface was sequentially abraded using emery papers of increasing grit size (220 to 1500), followed by final polishing on a rotating disc polisher until a mirror-like finish was achieved.

A 1 M HCl solution was prepared by diluting a standardized stock acid solution, which had been titrated against 0.1 M sodium carbonate solution using a volumetric method.

The corrosion inhibitor MK800 was dispersed in 1 M HCl at concentrations ranging from 50 to 800 ppm using an ultrasonicator for about 15–20 minutes. Electrochemical measurements were conducted at various temperatures (298–313 K) to assess the thermal stability and efficiency of the inhibitor under controlled conditions.

2.4 Electrochemical measurements

Electrochemical characterization of MS for corrosion behavior in 1 M HCl, both with and without the biomass-derived carbon nanosphere inhibitor (MK800), was performed using a CH660E electrochemical workstation (CH Instruments, USA). A conventional three-electrode configuration was employed, comprising a platinum as counter electrode, a saturated calomel as reference electrode (SCE), and MS as the working electrode. Prior to measurement, samples were stabilized under open-circuit potential (OCP) conditions for 400 s to ensure electrochemical equilibrium. EIS was performed at the stabilized OCP, while PDP measurements were carried out by sweeping the potential in the range of ± 250 mV relative to OCP at a scan rate of 1 mVs⁻¹. EIS and PDP measurements were each recorded in triplicate to ensure reproducibility and reliability of the data.

2.4.1 Potentiodynamic polarization studies. PDP experiments were performed at a constant scan rate of 1 mV s⁻¹, with the applied potential swept over a range of ± 250 mV around the open-circuit potential. The resulting Tafel plots were analyzed to determine the electrochemical parameters, including the corrosion current density (i_{corr}) and the Tafel slopes for the anodic ($+\beta_a$) and cathodic ($-\beta_c$) branches.

The corrosion rate (CR) was calculated using a standard formula (eqn (1)), which incorporates i_{corr} along with material-specific constants.

$$\text{CR} = \frac{3.272 \times M \times i_{\text{corr}}}{\rho \times Z} \quad (1)$$

In this equation, the factor 3.272 serves as a unit conversion constant, i_{corr} is the corrosion current density in A cm⁻², ρ represents the density of the metal (7.89 g cm⁻³), M is the

atomic mass of iron (55.5 g mol⁻¹), and Z , the number of electrons involved in the corrosion reaction, is assumed to be 2.

The surface coverage (θ), representing the fraction of the metal surface protected by the inhibitor, and the inhibition efficiency ($\eta\%$) were evaluated using eqn (2) and (3), respectively.

$$\theta = \frac{i_{\text{corr(B)}} - i_{\text{corr(I)}}}{i_{\text{corr(B)}}} \quad (2)$$

$$\eta_{\text{PDP}}(\%) = \frac{i_{\text{corr(B)}} - i_{\text{corr(I)}}}{i_{\text{corr(B)}}} \times 100 \quad (3)$$

These values were derived by comparing the corrosion current densities in the absence ($i_{\text{corr(B)}}$) and presence ($i_{\text{corr(I)}}$) of the MK800 inhibitor, both expressed in A cm⁻².

2.4.2 Electrochemical impedance spectroscopy measurements. EIS was performed in the frequency range of 100 kHz to 1 Hz with a 10 mV AC perturbation. Data analysis and equivalent circuit fitting were carried out using ZSimpWin 3.21 software, enabling the determination of polarization resistance (R_p) and double-layer capacitance (C_{dl}). The inhibition efficiency from EIS was calculated using the following equation:

$$\eta_{\text{EIS}}(\%) = \frac{R_{p(I)} - R_{p(B)}}{R_{p(I)}} \times 100 \quad (4)$$

where $R_{p(I)}$ and $R_{p(B)}$ are polarization resistance in the presence and absence of the inhibitor.

2.5 Surface analysis of MS

Surface analysis of MS under different treatment conditions was performed using SEM, OP, and WCA measurements. MS samples, including polished (bare), corroded (immersed in 1 M HCl), and inhibited (treated with MK800), were immersed in their respective solutions for 5 hours, then removed, dried, and exposed to ambient air for 24 hours prior to analysis. These samples were used to analyze SEM, OP, and WCA measurements. SEM imaging was conducted using a Carl Zeiss EVO10 instrument to examine morphological changes across the samples. Elemental analysis was carried out *via* EDS to determine surface composition. Surface roughness and topography were quantitatively evaluated by OP using a KLA Tencor instrument. The wettability of the samples was evaluated through WCA measurements. Water droplets (8 μ L) were carefully placed on the sample surfaces, and the droplet profiles were captured using a digital microscope equipped with a digital viewer. The contact angles were then quantified from the acquired images using the angle measurement tool in ImageJ software.

3 Results and discussion

3.1 Morphology and structural analysis

3.1.1 Thermogravimetric analysis (TGA). The thermogravimetric analysis (TGA) as presented in Fig. 1a, of the biomass precursor MK RAW reveals a characteristic two-step thermal degradation profile over the temperature range of 35 $^{\circ}$ C to 900 $^{\circ}$



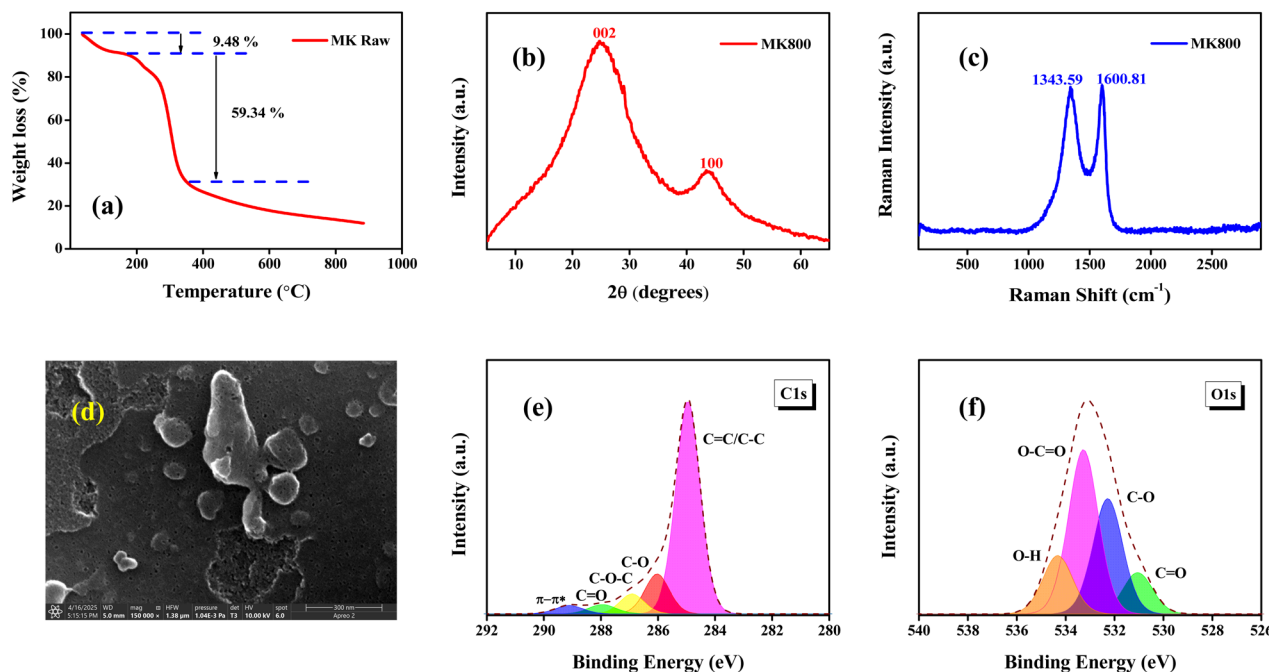


Fig. 1 (a) TGA of MK Raw; (b) XRD plot, (c) Raman spectra, and (d) FE-SEM image of MK800, and XPS deconvoluted C 1s spectra (e), and O 1s spectra (f) of MK800.

C at a controlled heating rate of 10 °C min^{-1} . An initial mass loss of approximately 9.48% occurs near 200 °C , predominantly due to the desorption of physically bound moisture. A subsequent and more pronounced weight reduction of around 59.34% is observed between 200 °C and 400 °C , and this is attributed to the thermal decomposition of structural biopolymers, including cellulose, hemicellulose, and lignin inherent in the biomass matrix. Above 400 °C , the rate of weight loss markedly decreases, indicating the formation of a more thermally stable carbonaceous structure. The stability of the material is confirmed by the absence of further significant mass changes at temperatures exceeding 800 °C , thereby validating the choice of 800 °C as the optimal pyrolysis temperature for the synthesis of CNS.³⁰

3.1.2 X-ray diffraction (XRD) and Raman analysis. X-ray diffraction (XRD) is an essential technique for determining the structural organization of materials. The graphitic character and the creation of highly ordered CNS are responsible for unique diffraction peaks ($2\theta = 24^\circ$ and 43°) in the XRD pattern, which correspond to the (002) and (101) planes (Fig. 1b).³¹

The Raman spectrum of the synthesized CNS exhibits two prominent peaks corresponding to the D and G bands are located at 1343.59 cm^{-1} and 1600.81 cm^{-1} (Fig. 1c). The A_{1g} mode of vibration is attributed to the disordered and structural defects arising from the sp^3 -hybridized carbon, which is represented by the D band. The E_{2g} mode of vibration is attributed to the sp^2 -linked carbon atoms in a graphitic layer, which is represented by the G band. The I_D/I_G ratio was found to be ≈ 0.84 , indicating a moderately ordered graphitic structure with the presence of structural defects.³²

3.1.3 FE-SEM, TEM analysis, and porosity studies. The morphology of the synthesized MK800 was analyzed by FESEM

(Fig. 1d), which revealed the presence of spherical carbon nanoparticles with minor surface irregularities, likely contributing to their tendency to aggregate. The average particle size of MK800 was estimated to be approximately $60\text{--}70\text{ nm}$. EDS analysis confirmed carbon as the predominant element (83.9%), accompanied by oxygen (10.4%), and trace amounts of potassium (4.0%), phosphorus (1%), and magnesium (0.6%), as shown in Fig. S1. TEM imaging (Fig. S2) further validated the spherical morphology, providing a closer view of the overall structural consistency.

The surface area and porosity of MK800 were evaluated through N_2 adsorption–desorption isotherm analysis at 77 K (Fig. S3a). The isotherm exhibited type IVa characteristics with a pronounced hysteresis loop, confirming a mixed micro- and mesoporous structure. MK800 showed a high specific surface area of $1090.2\text{ m}^2\text{ g}^{-1}$ and a total pore volume of $0.5\text{ cm}^3\text{ g}^{-1}$. The pore size distribution was determined using the Barrett–Joyner–Halenda (BJH) method (Fig. S3b), revealing an average pore diameter of approximately $1.9\text{--}2.0\text{ nm}$, suggesting mesoporous nature of the materials which has been reported in our previous study.²⁹

3.1.4 X-ray photoelectron spectroscopy (XPS) analysis. X-ray photoelectron spectroscopy (XPS) analysis of MK800 provides valuable insights into its surface composition and chemical functionality. The survey-scan XPS spectrum (Fig. S4) displays two dominant peaks corresponding to carbon (C 1s at 285 eV) and oxygen (O 1s at 533 eV), confirming the presence of only carbon- and oxygen-containing species. The high-resolution C 1s spectrum (Fig. 1e) reveals multiple deconvoluted peaks at 285.0 , 286.0 , 286.9 , 288.0 , and 289.1 eV . These are assigned to C–C/C=C, C–O, C–O–C, C=O, and $\pi\text{--}\pi^*$ shake-up satellite transitions, respectively, indicating the coexistence of



both sp^2 and oxygenated carbon species on the surface.³³ The corresponding O 1s spectrum (Fig. 1f) exhibits four distinct peaks at 531.1, 532.3, 533.3, and 534.3 eV which are attributed to C=O, C-O, O-C=O, and -OH functionalities, respectively.³⁴ The relative intensities of the C 1s and O 1s peaks further suggest a surface rich in carbon with significant oxygen-containing functional groups, which can play a crucial role in influencing the nanomaterial's reactivity and interaction with its environment.

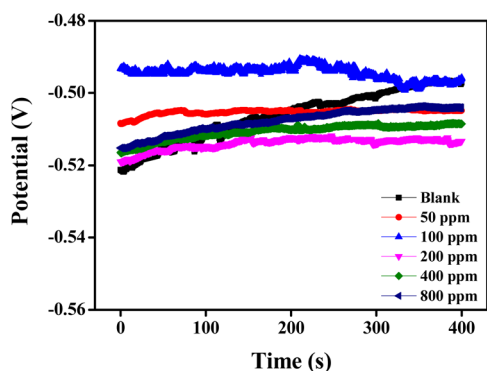


Fig. 2 Open-circuit potential (OCP) versus time curves for mild steel in 1 M HCl in the absence and presence of different concentrations of MK800 at 308 K.

3.2 Electrochemical studies

3.2.1 Open circuit potential. OCP measurements serve as a fundamental, non-invasive technique to assess the thermodynamic tendency of a metal surface to undergo corrosion in a given environment. The evolution of OCP over time offers insight into the electrochemical stability of the system and the interaction of inhibitor molecules with the metal surface.³⁵ Prior to PDP or EIS, recording OCP ensures the system reaches quasi-equilibrium, which is essential for reliable interpretation of further electrochemical data.³⁶ OCP measurements were employed to investigate the time-dependent electrochemical behavior of MS in 1 M HCl, with and without the addition of MK800, a biomass-derived CNS inhibitor.

The OCP was recorded for 400 s, as a quasi-steady state was achieved within this time and no significant change in potential was observed thereafter. As shown in Fig. 2, the OCP curves exhibited a stable trend over this period, indicating the attainment of quasi-equilibrium conditions and the absence of passivating oxide film formation. In the presence of MK800, the OCP exhibits only a slight positive shift, whereas the blank shows a more pronounced increase, indicating that MK800 acts as a mixed-type inhibitor by simultaneously suppressing anodic metal dissolution and cathodic hydrogen evolution without significantly altering the corrosion mechanism.⁴ The slight variations in OCP observed with the change in inhibitor concentration are attributed to the gradual equilibration of the

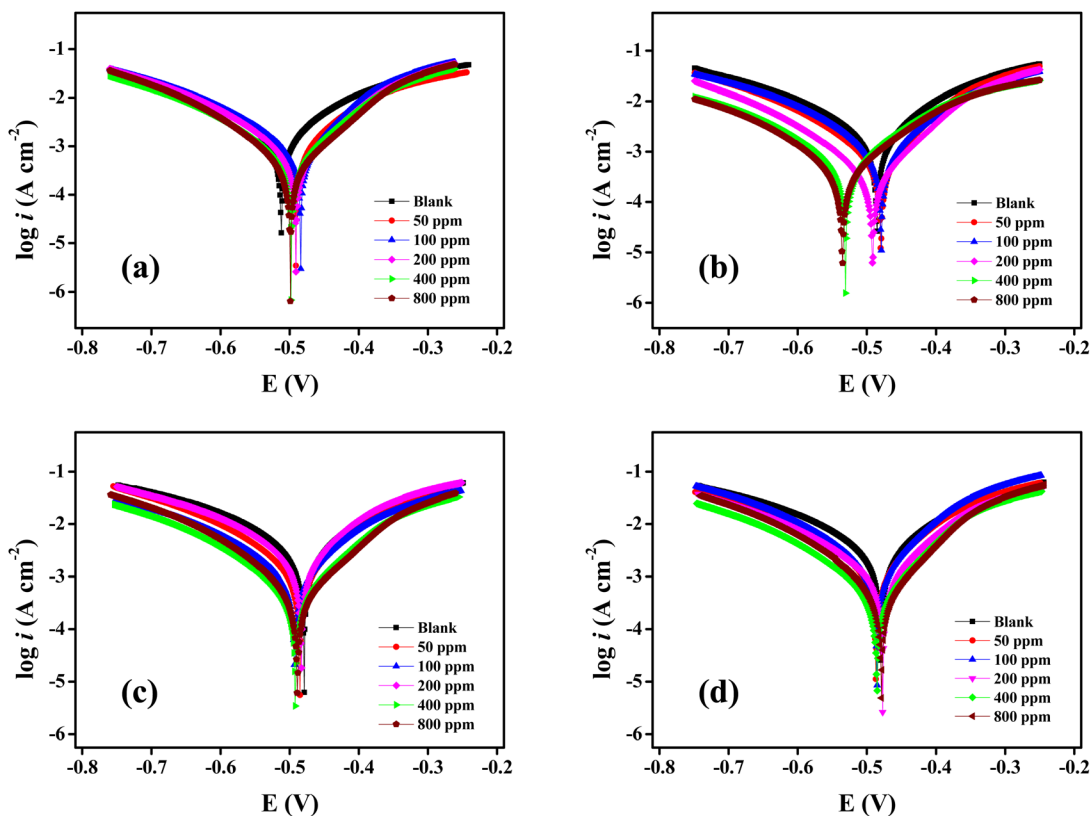


Fig. 3 Tafel polarization plots for mild steel in 1 M HCl at different concentrations of MK800 recorded at (a) 298 K, (b) 303 K, (c) 308 K, and (d) 313 K.



metal-electrolyte interface and the progressive adsorption of MK800 molecules. The enhanced OCP stability at higher concentrations, particularly at 800 ppm, suggests the formation of a uniform and protective adsorbed layer on the mild steel surface.

3.2.2 Potentiodynamic polarization measurements. The electrochemical performance of MK800, a biomass-derived carbon nanospheres inhibitor, was assessed through PDP studies. PDP tests were performed on MS specimens immersed in 1 M HCl, with varying concentrations of the MK800 inhibitor ranging from 50 to 800 ppm, and at different temperatures between 298 K and 313 K. As shown in Fig. 3, the polarization curves reveal a substantial decline in both anodic and cathodic current densities upon the addition of MK800, indicating suppression of both metal dissolution and hydrogen evolution reactions. The corrosion current densities were quantified using the Tafel extrapolation method, and corrosion inhibition efficiency was calculated using the standard equation based on the difference between uninhibited and inhibited current densities (eqn (3)).^{37,38} Increasing MK800 concentration from 50–800 ppm enhanced the inhibition efficiency, suggesting a concentration-dependent surface coverage effect. Notably, the cathodic branches of the Tafel plots remained nearly parallel across all concentrations, implying that MK800 functions *via* a mixed-type inhibition mechanism without altering the reaction pathway, consistent with the behaviour of carbon-based inhibitors reported in literature.^{20,39}

The polarization curves show a gradual decrease in corrosion current density (i_{corr}) with increasing MK800 concentration relative to the uninhibited solution, indicating improved corrosion resistance of MS due to the formation of a surface-

protective layer. The consistent shape of both the anodic and cathodic branches across all temperatures and MK800 concentrations suggests that the core corrosion processes: iron oxidation at the anode and hydrogen evolution at the cathode, remain fundamentally unaltered. This invariance in Tafel slope geometry further confirms that MK800 does not significantly influence the kinetics or mechanisms of electrochemical half-reactions. According to literature survey, a shift in corrosion potential (E_{corr}) exceeding ± 85 mV typically indicates a predominantly anodic or cathodic inhibition mechanism. However, if the shift remains within ± 85 mV, the inhibitor is categorized as exhibiting mixed-type behavior.⁴⁰ In this study, E_{corr} shifts remain below ± 85 mV across the temperature range, confirming the mixed-type inhibition nature of MK800.

The key electrochemical parameters, such as E_{corr} , corrosion current density (i_{corr}), anodic and cathodic Tafel slopes ($+\beta_a$ and $-\beta_c$), corrosion rate (CR), and inhibition efficiency ($\eta\%$), were extracted by extrapolating the Tafel lines and are summarized in Table 1. In the absence of the inhibitor, E_{corr} shifts positively with increasing temperature, highlighting thermal effects on corrosion kinetics. Meanwhile, the addition of MK800 leads to a noticeable decline in both i_{corr} and CR values, with increasing inhibitor concentration enhancing the inhibition efficiency. The MK800 inhibitor demonstrates increasing effectiveness with rising concentration and temperature, achieving a maximum inhibition efficiency of approximately 83.8% at 800 ppm and 313 K. The observed decrease in the corrosion rate (CR) without a significant shift in the corrosion potential (E_{corr}) upon the addition of MK800 indicates that the inhibitor exhibits the characteristic behavior of a pickling-type inhibitor.⁴

Table 1 Tafel parameters for MS in 1 M HCl medium at different concentrations and temperatures

Temp. (K)	Conc. of MK800 (ppm)	E_{corr} (V)	i_{corr} (10^{-5}) (A cm^{-2})	$-\beta_c$ (mV dec^{-1})	$+\beta_a$ (mV dec^{-1})	CR (mpy)	IE (%)
298	Blank	-0.5139	184.2	163.96	131.85	833.6	—
	50	-0.4919	119.2	154.96	119.74	539.4	35.3 \pm 0.58
	100	-0.4849	96.2	141.24	91.00	435.4	47.8 \pm 0.91
	200	-0.4945	64.5	119.67	96.64	292.0	65.0 \pm 1.22
	400	-0.4962	51.4	119.24	98.56	232.6	72.1 \pm 1.56
	800	-0.4991	39.8	107.96	93.20	179.9	78.4 \pm 1.16
303	Blank	-0.4856	206.3	160.82	124.25	933.7	—
	50	-0.4767	125.3	131.56	108.51	567.1	39.3 \pm 0.93
	100	-0.4935	103.1	132.85	110.50	466.5	50.0 \pm 1.59
	200	-0.5016	70.9	136.85	113.43	325.2	65.7 \pm 1.40
	400	-0.5402	56.4	131.35	121.55	255.3	72.7 \pm 0.97
	800	-0.5444	43.0	125.09	115.83	194.6	79.2 \pm 1.19
308	Blank	-0.4852	254.2	169.69	137.15	1150.0	—
	50	-0.4853	141.4	132.11	108.04	639.8	44.4 \pm 0.70
	100	-0.4932	119.8	155.40	113.08	542.4	52.9 \pm 1.03
	200	-0.5067	84.1	130.27	100.32	380.6	66.2 \pm 1.48
	400	-0.4858	61.4	122.15	99.76	277.8	75.9 \pm 1.44
	800	-0.4897	48.7	112.23	101.97	220.2	80.9 \pm 1.52
313	Blank	-0.4809	305.2	164.74	134.03	1382.0	—
	50	-0.4878	144.9	147.31	106.68	655.8	52.5 \pm 1.43
	100	-0.4858	140.2	130.89	95.84	639.7	54.1 \pm 1.51
	200	-0.4780	96.9	130.68	97.75	438.5	68.3 \pm 1.83
	400	-0.4839	74.4	125.62	112.09	336.7	75.6 \pm 0.87
	800	-0.4860	49.3	115.99	89.57	223.1	83.9 \pm 1.61



The obtained results reveal that MK800 effectively inhibits the corrosion of MS in 1 M HCl by occupying active sites on the surface and promoting the development of a protective film. This adsorbed layer impedes the interaction between the metal and the corrosive medium, thereby reducing the rate of electrochemical processes.⁴¹

3.2.3 Electrochemical impedance spectroscopy. EIS was employed to evaluate the corrosion behaviour of MS in 1 M HCl at various MK800 inhibitor concentrations (50–800 ppm) and temperatures (298–313 K), as shown in Fig. 5. The impedance

results were found to be in good agreement with those obtained from PDP measurements, confirming the consistency of the electrochemical data. Nyquist plots for the blank and inhibited systems display a single depressed capacitive semicircle in both cases, typical of charge transfer-controlled corrosion processes. The depressed nature of the semicircles is commonly associated with surface heterogeneity, roughness, and non-uniform adsorption of the inhibitor on the metal surface.^{42,43} The diameter of the semicircles increases with inhibitor concentration at all studied temperatures, indicating enhanced

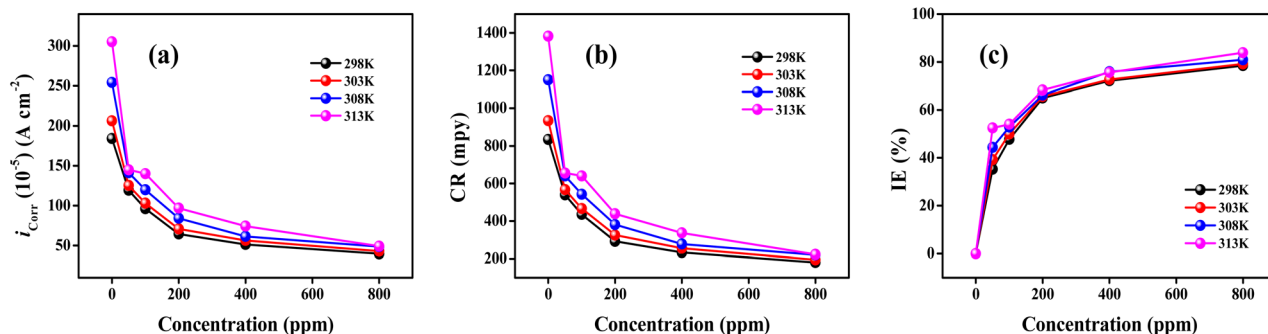


Fig. 4 Effects of varying concentration of MK800 and temperature of the media on corrosion parameters: (a) i_{corr} , (b) CR, and (c) inhibition efficiency (IE%).

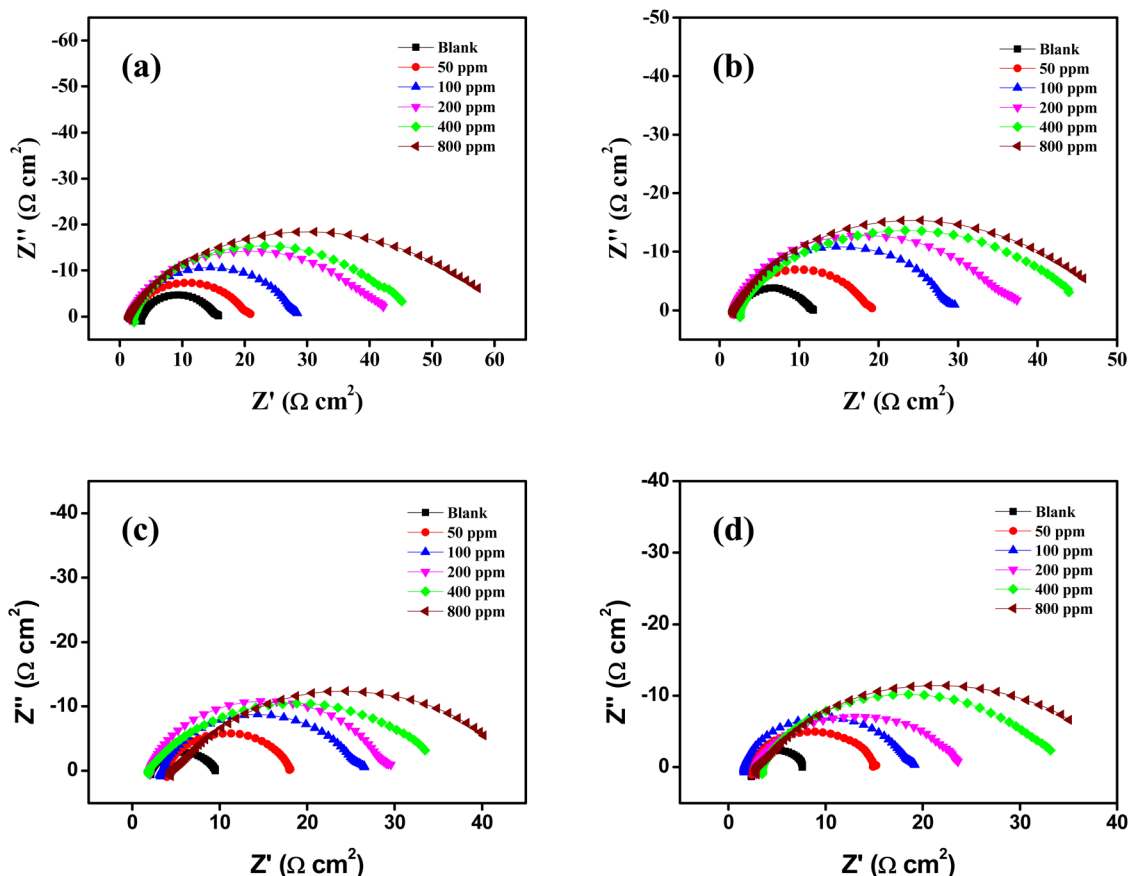


Fig. 5 Nyquist plots for mild steel in 1 M HCl at different concentrations of MK800 recorded at (a) 298 K, (b) 303 K, (c) 308 K, and (d) 313 K.



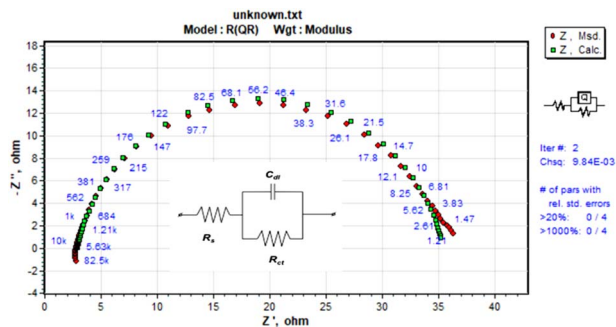


Fig. 6 Fitted impedance plot for mild steel in 1 M HCl containing 200 ppm of MK800 at 303 K, with the equivalent electrical circuit shown in the inset.

resistance to charge transfer due to the formation of a protective inhibitor layer. The presence of a single semicircle in the Nyquist plot suggests that both anodic and cathodic processes are governed by a common charge-transfer mechanism, indicating mixed-type inhibition behavior.⁴⁴

To quantitatively interpret the EIS data, an appropriate equivalent circuit model was fitted based on the shape of the Nyquist plots and the complexity of the interfacial reactions. The equivalent circuit used for fitting, a simplified Randles-type circuit ($R(QR)$), is shown in the inset of Fig. 6 and was employed to model both the uninhibited and inhibited systems. The circuit includes the solution resistance (R_s), polarization resistance (R_p – equivalent to charge transfer resistance), and a constant phase element (CPE) to account for non-ideal capacitive behaviour, replacing the traditional double-layer

capacitance (C_{dl}). Using this model, the key electrochemical parameters were reliably extracted and are summarized in Table 2.

The solution resistance (R_s) values show only minor variations with the addition of MK800 and temperature, indicating that the presence of the inhibitor does not significantly alter the conductivity of the bulk electrolyte. This confirms that the observed changes in corrosion behavior mainly arise from interfacial processes rather than from changes in the solution properties.

The polarization resistance (R_p) was observed to increase with inhibitor concentration at all temperatures, indicating enhanced corrosion protection due to the formation of a protective adsorbed film. A slight decrease in R_p with increasing temperature suggests thermally influenced desorption of the inhibitor molecules, leading to a partial reduction in inhibition efficiency. The impedance of the CPE was calculated using eqn (5),⁴⁵

$$Z_{CPE} = Y_0^{-1}(j\omega)^{-n} \quad (5)$$

where Y_0 is the admittance constant, ω is the angular frequency, j is the imaginary unit, and n is the phase shift exponent ranging from 0 to 1. When $n = 1$, the CPE behaves as an ideal capacitor.⁴⁶ The obtained n values being lower than unity indicate non-ideal capacitive behavior, which arises from surface roughness, heterogeneity, and non-uniform distribution of active sites on the MS surface. The fact that the n values remain close to that of the blank solution, with only slight variations, suggests that the interfacial mechanism is preserved and that

Table 2 EIS parameters for MS in 1 M HCl medium at different concentrations and temperatures

Temp. (K)	Conc. of MK800 (ppm)	R_s (Ω cm ²)	n	R_p (Ω cm ²)	C_{dl} (μ F cm ²)	IE (%)
298	Blank	3.599	0.8761	11.71	65.41	—
	50	2.077	0.8867	18.08	64.09	35.3 ± 0.43
	100	1.867	0.8902	25.87	64.01	54.7 ± 0.85
	200	1.651	0.8492	38.77	62.60	69.8 ± 1.18
	400	2.284	0.8353	46.16	58.52	74.6 ± 0.61
	800	1.542	0.7740	55.24	55.68	78.8 ± 1.02
303	Blank	2.233	0.8638	9.21	67.57	—
	50	1.691	0.9061	16.78	65.27	45.1 ± 0.67
	100	2.075	0.8771	26.69	64.91	65.5 ± 0.80
	200	1.829	0.8622	33.77	63.06	72.7 ± 0.81
	400	2.608	0.7809	40.89	60.14	77.5 ± 0.71
	800	1.772	0.7739	45.15	57.05	79.6 ± 0.97
308	Blank	2.191	0.8736	7.17	105.10	—
	50	3.995	0.897	13.92	72.86	48.5 ± 1.02
	100	3.409	0.8651	22.52	67.12	68.2 ± 0.70
	200	2.549	0.9125	26.84	65.50	73.1 ± 0.76
	400	1.851	0.8741	32.58	61.73	78.0 ± 0.96
	800	2.792	0.8868	42.87	58.94	83.3 ± 1.20
313	Blank	2.491	0.9546	5.11	109.00	—
	50	2.406	0.8668	12.58	80.09	59.4 ± 0.92
	100	2.837	0.8714	16.97	75.85	69.9 ± 1.01
	200	2.881	0.7901	20.61	73.51	75.2 ± 1.17
	400	3.485	0.7766	29.85	69.47	82.9 ± 1.58
	800	2.978	0.6683	39.58	64.82	87.1 ± 1.48



MK800 adsorption does not significantly alter the fundamental capacitive nature of the interface.

The double-layer capacitance (C_{dl}) was determined using eqn (6),

$$C_{dl} = Y_0(\omega_{max})^{n-1} \quad (6)$$

where ω_{max} represents the frequency at which the imaginary component of impedance is maximum. A consistent decline in C_{dl} with increasing MK800 concentration was observed, indicating a thicker electrical double layer at the metal-electrolyte interface. This reduction is attributed to the effective inhibitor adsorption of inhibitor molecules, which displace water molecules and other ions, leading to a decrease in the local dielectric

constant and the formation of a protective adsorbed layer.⁴⁷ In contrast, for a given MK800 concentration, C_{dl} increases with temperature, which can be attributed to enhanced mobility and rearrangement of the inhibitor molecules at the metal-electrolyte interface.

The inhibition efficiency was calculated from the R_p values using eqn (4), further supporting the protective action of MK800 through its effective adsorption onto the MS surface in the acidic environment. The corresponding inhibition efficiencies ranged from 35.3% to 87.1% in 1 M HCl, confirming the concentration-dependent protective effect of MK800 on the MS surface.

The Bode plots (Fig. 8) for MS in 1 M HCl reveal a notable increase in phase angle with rising concentrations of MK800.

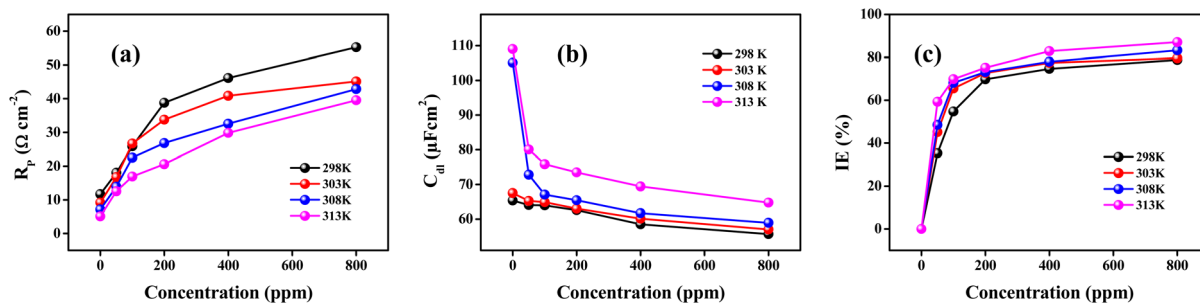


Fig. 7 Effects of varying concentration of MK800 and temperature of the media on corrosion parameters: (a) R_p , (b) C_{dl} , and (c) inhibition efficiency (IE %).

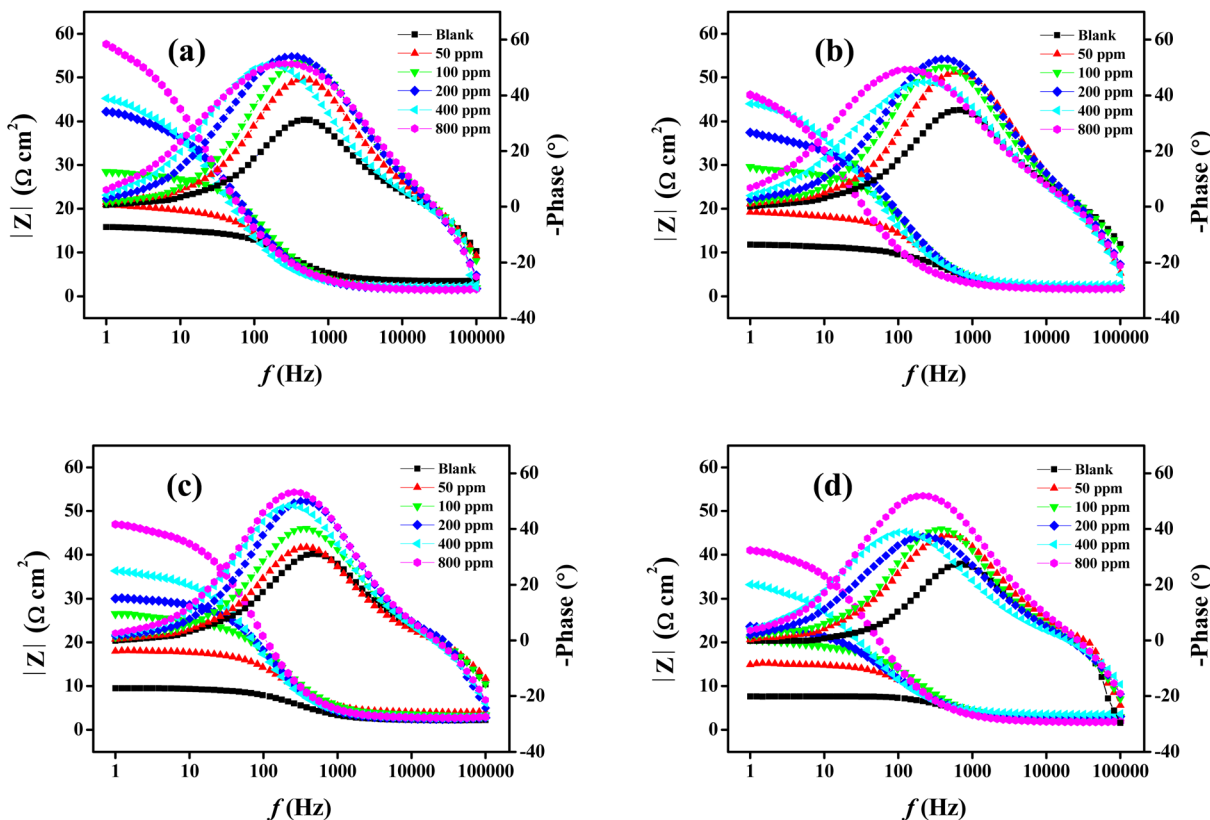


Fig. 8 Bode modulus and Bode phase plots for mild steel in 1 M HCl at different concentrations of MK800 recorded at (a) 298 K, (b) 303 K, (c) 308 K, and (d) 313 K.



This trend, also summarized in Table 2, indicates a progressive reduction in capacitive behaviour at the metal-electrolyte interface, which is associated with a lower rate of metal dissolution. The polarization resistance (R_p), estimated from the difference between the high-frequency (HF) and low-frequency (LF) regions of the Bode plots, was observed to increase with inhibitor concentration. This rise in R_p suggests enhanced surface protection due to a combination of suppressed metal dissolution and improved passivation, along with increased electrical resistance of the inhibitor film at the interface.⁴⁸

The influence of inhibitor concentration and temperature on corrosion performance reveals key mechanistic behavior of nanoparticle-based systems. An increase in CNS concentration (50–800 ppm) resulted in improved surface coverage and inhibition efficiency, supported by both EIS and PDP measurements, which can be attributed to increased adsorption and the formation of a more uniform protective film.⁴⁹ Similarly, the impact of temperature presents a dual-effect phenomenon. Higher temperatures increase the kinetic energy of ions in solution, enhancing their diffusion toward the metal surface and thus accelerating corrosion processes.⁵⁰ This trend is typically reflected by a decrease in polarization resistance (R_p) (from 298–313 K) (Fig. 7a). However, elevated temperatures also improve the mobility and diffusivity of inhibitor molecules, enabling better access to the metal surface, thereby facilitating stronger adsorption and leading to improved surface coverage in the electrochemical system.⁵¹ This observation is supported by the increase in inhibition efficiency with rising temperature across all concentrations (Fig. 4c and 7c). These findings highlight the critical role of both inhibitor concentration and temperature of the experimental system in governing the stability and efficacy of the protective film.

For comparative evaluation, Table 3 summarizes the corrosion inhibition efficiency of CNS (MK800) alongside those reported in the literature for other carbon-based nanomaterials.

3.3 Adsorption isotherm and thermodynamic studies

Numerous studies have demonstrated that the inhibitory performance of corrosion inhibitors is primarily attributed to their adsorption on the metal surface. Accordingly, adsorption

isotherm analysis offers essential insight into the nature and strength of the interactions between inhibitor molecules and the MS surface. To elucidate the adsorption behaviour of MK800 on MS, several isotherm models were evaluated, including the Langmuir, Temkin, and Freundlich models. The surface coverage (θ) (from eqn (7)) was calculated using inhibition efficiencies obtained from Tafel polarization measurements across various inhibitor concentrations. These θ values were then fitted to the respective adsorption models to assess the adsorption mechanism.

Graphical evaluation of the adsorption data is presented in Fig. 9a–c, corresponding to Langmuir, Freundlich, and Temkin plots, respectively. Among these, the Langmuir isotherm provided the best linear fit, as evidenced by the near-unity slope in the C_{inh}/θ versus C_{inh} plot (Fig. 9a) and a correlation coefficient (R^2) approaching 1. This suggests that MK800 adsorption onto the MS surface adheres to the Langmuir model, which assumes homogeneous surface adsorption with identical energy sites and monolayer coverage, without lateral interaction among adsorbed molecules.^{60,61}

$$\frac{C_{\text{inh}}}{\theta} = \frac{1}{K} + C_{\text{inh}} \quad (7)$$

In the Langmuir model, C_{inh} denotes the inhibitor concentration, θ represents the fraction of surface coverage, and K is the equilibrium adsorption constant. The value of K was determined from the intercept of the linear plot and was subsequently used to compute the standard free energy of adsorption ($\Delta G_{\text{ads}}^\circ$) via the following relation:

$$\Delta G_{\text{ads}}^\circ = -RT \ln(K \times 55.5) \quad (8)$$

Here, R is the universal gas constant, T is the temperature in Kelvin, and 55.5 is the molar concentration of water in the solution (mol L^{-1}). The magnitude and sign of $\Delta G_{\text{ads}}^\circ$ provide insight into the nature of the adsorption process. It is widely accepted that values around -20 kJ mol^{-1} indicate physisorption, while values approaching -40 kJ mol^{-1} suggest chemisorption.^{62,63} As reported in Table 3, the $\Delta G_{\text{ads}}^\circ$ values for MK800 are close to -20 kJ mol^{-1} , implying that the inhibition

Table 3 Comparison of the corrosion inhibition efficiency of CNS with other carbon-based nanomaterials reported in the literature in HCl medium

Nanoparticles	Conc. of inhibitor used	Medium	Metal used	Temp. of the medium	Inhibition efficiency	References
NiO-modified activated carbon	NA	1 M HCl	Mild steel	298 K	38.59%	52
Mixed metal oxides (Cu,Zn, NiO) NPs/rGO	500 ppm	0.1 M HCl	Mild steel	298 K	80%	53
Polyaniline tannate (PANI-TA) modified functionalized CNT	75 ppm	1 M HCl	Mild steel	298 K	90.6%	54
Chitosan-based CDs	40 ppm	1 M HCl	Mild steel	298 K	97.4%	55
N-CDs	200 ppm	1 M HCl	Q235 steel	298 K	90%	56
Biomass-derived CQDs	200 ppm	1 M HCl	Q235 steel	298 K	95.98%	57
Biomass-derived CQDs	500 ppm	1 M HCl	Mild steel	303 K	90.9%	58
Biochar	200 ppm	1 M HCl	Mild steel	303 K	80.2%	59
Biomass-derived CNS (MK800)	800 ppm	1 M HCl	Mild steel	313 K	87.1%	Present work



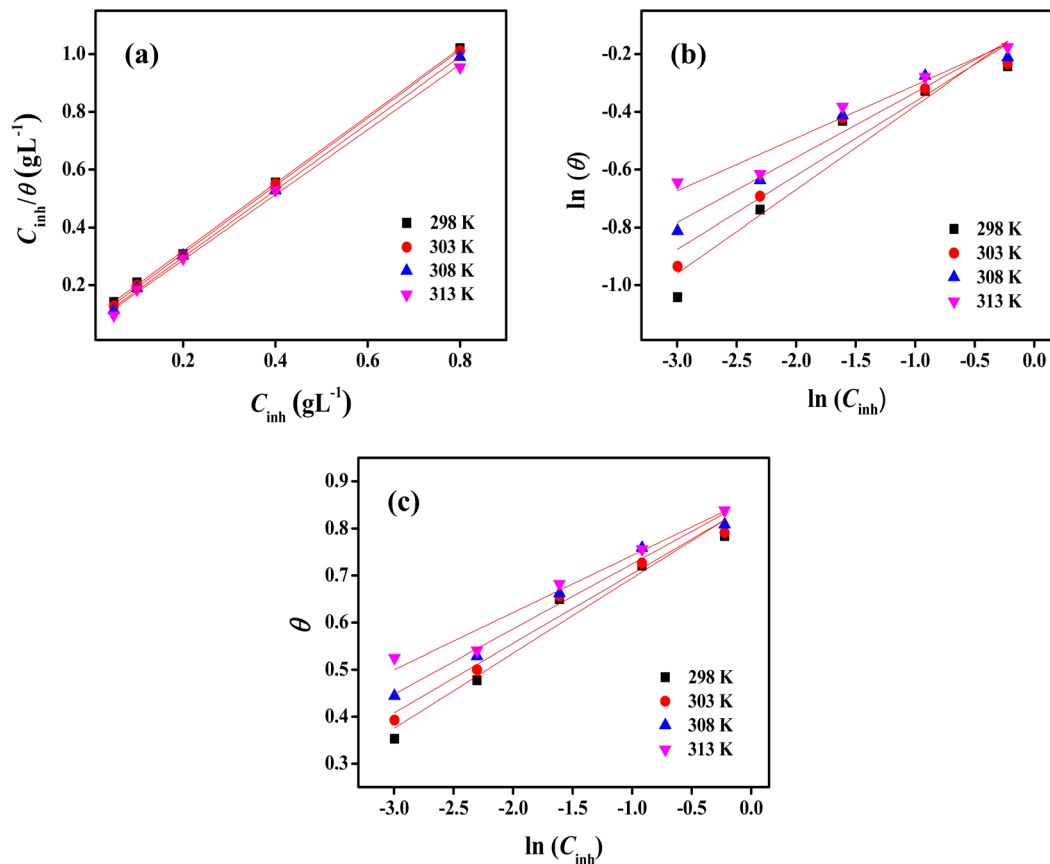


Fig. 9 Adsorption isotherms: (a) Langmuir, (b) Freundlich, and (c) Temkin isotherm plots for MK800 on MS in 1 M HCl.

mechanism primarily involves spontaneous physical adsorption of the inhibitor molecules onto the MS surface.

The thermodynamic parameters associated with the adsorption of MK800 on MS were further evaluated by calculating the standard enthalpy ($\Delta H_{\text{ads}}^{\circ}$) and entropy ($\Delta S_{\text{ads}}^{\circ}$) of adsorption using eqn (9). A linear plot of $\Delta G_{\text{ads}}^{\circ}$ versus temperature (T), shown in Fig. 10, was used for this analysis. The slope and intercept of this plot provided the corresponding values of $\Delta H_{\text{ads}}^{\circ}$ and $\Delta S_{\text{ads}}^{\circ}$, as summarized in Table 4. The positive value

of $\Delta H_{\text{ads}}^{\circ}$ ($16.387 \text{ kJ mol}^{-1}$) indicates that the adsorption of MK800 onto the steel surface in 1 M HCl is an endothermic process,⁶⁴ suggesting increased inhibitor adsorption with rising temperature.

$$\Delta G_{\text{ads}}^{\circ} = \Delta H_{\text{ads}}^{\circ} - T\Delta S_{\text{ads}}^{\circ} \quad (9)$$

3.4 Effect of temperature and kinetic studies

To investigate the temperature-dependent kinetics of MS corrosion in 1 M HCl, PDP measurements were performed in both inhibited and blank solutions over the temperature range of 298–313 K. The results revealed that the corrosion rate increased with rising temperature in both media, likely due to reduced hydrogen overpotential, while increasing concentrations of MK800 significantly suppressed the corrosion rate. To gain further insight into the corrosion mechanism, the Arrhenius equation was applied to evaluate the activation energy (E_a) of the corrosion process:

$$\ln(\text{CR}) = B - \frac{E_a}{RT} \quad (10)$$

where CR is the corrosion rate, B is the Arrhenius pre-exponential factor, R is the universal gas constant, and T is the absolute temperature.

A plot of $\ln(\text{CR})$ versus $1/T$ (Fig. 11a) produced a straight line whose slope ($-E_a/R$) was used to calculate the activation energy

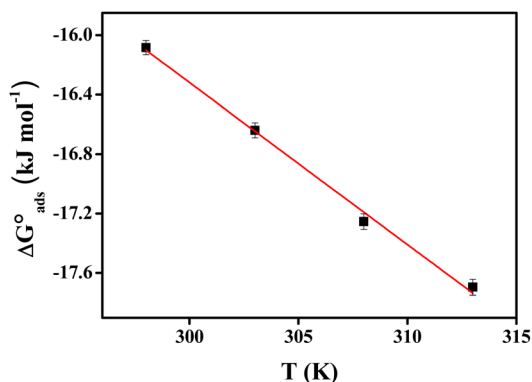
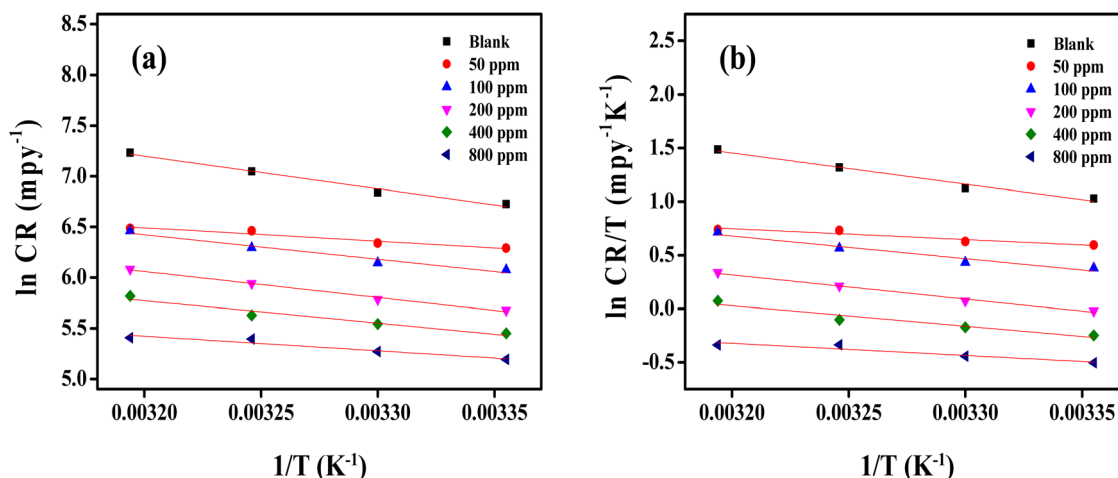


Fig. 10 Adsorption plot of $\Delta G_{\text{ads}}^{\circ}$ vs. T for MS in the presence of inhibitor in 1 M HCl.



Table 4 Thermodynamic parameters measured for 1 M HCl

Temp. (K)	$\Delta G_{\text{ads}}^{\circ}$ (kJ mol ⁻¹)	R^2	Slope	$\Delta H_{\text{ads}}^{\circ}$ (kJ mol ⁻¹)	$\Delta S_{\text{ads}}^{\circ}$ (kJ mol ⁻¹ K ⁻¹)
298	-16.101	0.99953	1.1696		
303	-16.646	0.99956	1.1725	16.387	-0.1090
308	-17.191	0.99944	1.1559		
313	-17.736	0.99713	1.1271		

Fig. 11 (a) $\ln(\text{CR})$ vs. $(1/T)$ plot (Arrhenius plot), and (b) $\ln(\text{CR})/T$ vs. $(1/T)$ plot (Transition state equation) for MS in studied concentrations and temperature in 1 M HCl.

values at different inhibitor concentrations (Table 5). These results indicate that the inhibitor promotes effective surface coverage, thereby suppressing the corrosion process and contributing to improved metal stability at higher temperatures.^{65,66}

Additionally, the transition state theory was employed to compute the activation enthalpy (ΔH_a) and entropy (ΔS_a) using the following equation:

$$\text{CR} = \frac{RT}{Nh} \exp\left(\frac{\Delta S_a}{R}\right) \exp\left(\frac{\Delta H_a}{RT}\right) \quad (11)$$

where N is Avogadro's number and h is Planck's constant. The linear plot of $\ln(\text{CR}/T)$ against $1/T$ (Fig. 11b) yielded slopes and intercepts from which ΔH_a and ΔS_a were extracted. The positive enthalpy values confirm that the dissolution of MS is endothermic in nature. Meanwhile, the large negative ΔS_a values

observed in both inhibited and uninhibited systems suggest a highly ordered activated complex, consistent with an associative mechanism where reactant molecules lose degrees of freedom as they transition to the activated state.^{67,68}

These thermodynamic parameters collectively support the proposed adsorption mechanism of MK800 on the MS surface and affirm the efficacy of MK800 as a temperature-stable, surface-active corrosion inhibitor.

3.5 Surface characteristics

3.5.1 SEM-EDS analysis. Fig. 12a–c represents the SEM micrographs illustrating the surface morphology of MS specimens under varying corrosive conditions. Fig. 12a corresponds to the freshly polished specimen, revealing a uniform and defect-free surface with discernible grinding lines from pre-treatment. Upon exposure to a 1 M HCl solution, severe surface degradation, which is evident in Fig. 12b, characterized by extensive pitting, cracks, and localized dissolution, is attributable to the aggressive chloride ions. The observation is consistent with previous corrosion studies in acidic media.⁶⁹ However, the introduction of 800 ppm of the synthesized inhibitor significantly mitigates corrosion, as shown in Fig. 12c; the surface exhibits a marked reduction in roughness and defect density, indicating effective surface protection. Complementary EDS analysis (Fig. S5a–c) (Table 6) revealed a substantial increase in carbon signals in the inhibited sample, suggesting the formation of an adsorbed inhibitor film.⁷⁰ Furthermore, a higher percentage of iron and a lower

Table 5 Activation parameters (E_a) measured for the MS in 1 M HCl before and after the addition of the MK800 inhibitor

Conc. MK800 (ppm)	E_a (kJ mol ⁻¹)	ΔH_a (kJ mol ⁻¹)	ΔS_a (J mol ⁻¹ K ⁻¹)
Blank	26.674	24.141	-108.203
50	10.957	8.423	-164.370
100	20.160	17.626	-135.485
200	21.304	18.770	-134.843
400	18.437	15.903	-146.407
800	11.940	9.405	-170.116



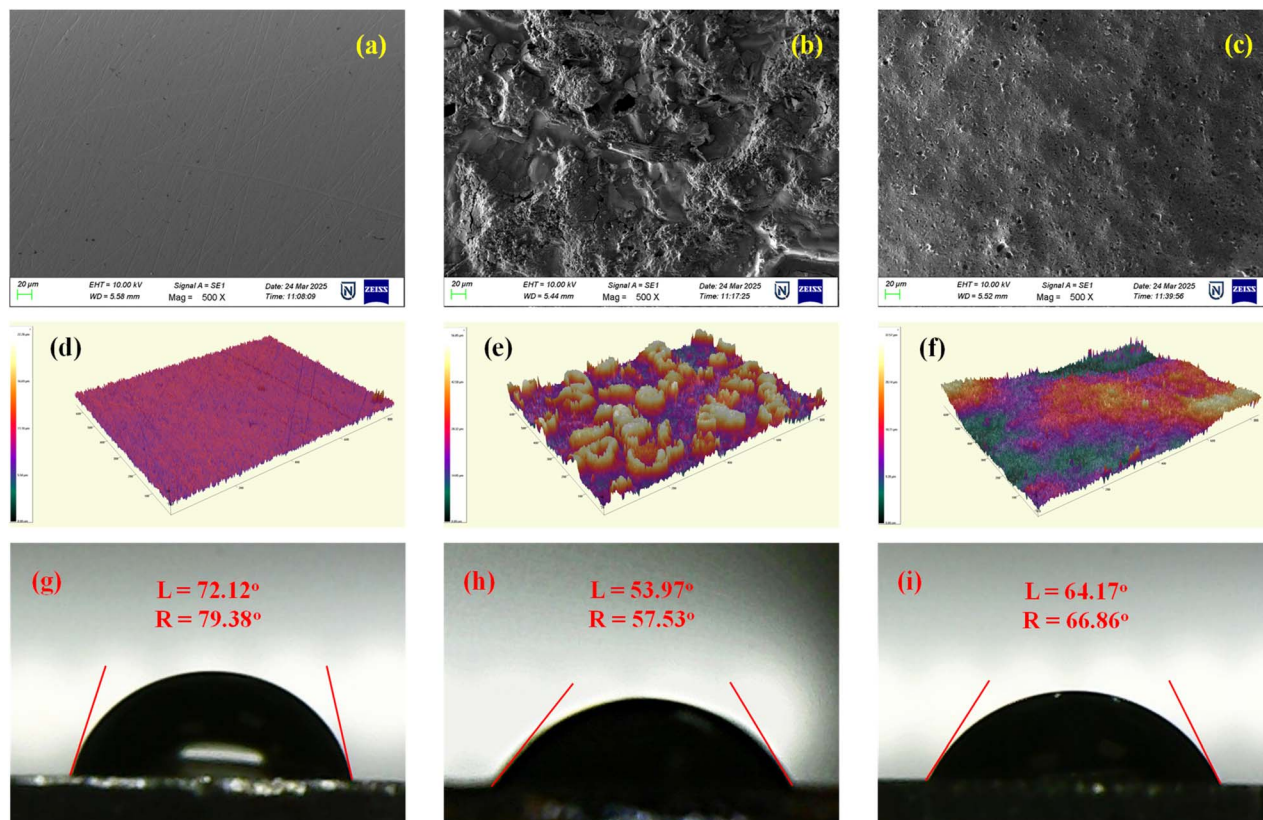


Fig. 12 SEM images (a–c), Optical profilometer images (d–f), and Water contact angle measurements (g–i) of polished, uninhibited, and inhibited MS samples, respectively.

Table 6 The atomic composition from EDS analysis

Samples	Atomic composition (%)							
	Al	P	Mn	Si	O	C	Cl	Fe
MS								
Bare	0.09	0.1	0.18	0.9	0.62	2.04	—	96.16
1 M HCl	—	—	—	—	24.37	0.78	25.18	49.67
1 M HCl + MK800	—	—	—	—	31.83	8.59	2.98	56.60

percentage of chlorine on the surface in the inhibited specimen compared to the acid-only sample indicated lower material loss and better substrate preservation.⁷¹

3.5.2 Optical profilometry. Fig. 12d–f illustrates the surface topography of MS specimens subjected to 1 M HCl immersion, as analyzed by optical profilometry (OP). The polished MS surface (Fig. 12d) exhibits uniformity with minimal height variation, while Fig. 12e reveals significant surface deterioration due to acid exposure, manifested as deep valleys and

Table 7 Roughness parameters from the optical profilometer

Specimens	R_a (μm)	R_q (μm)
MS polished	0.8786	1.113
MS in 1 M HCl	3.777	5.482
MS in 1 M HCl + MK800	1.784	2.284

pronounced peaks, hallmarks of corrosive attack and the formation of corrosion products.⁷² Remarkably, the introduction of 800 ppm of MK800 inhibitor resulted in substantial improvement in surface uniformity, as seen in Fig. 12f. Quantitative assessment of roughness parameters (Table 7) revealed that average roughness (R_a) and root mean square roughness (R_q) values were markedly reduced in the inhibited sample compared to the acid-only condition, confirming the presence of a protective inhibitor film. This protective film restricts access of corrosive ions to the metallic substrate, thereby minimizing surface damage. Furthermore, these results are corroborated by EDS and SEM analyses, which indicate a notable retention of surface integrity and elemental uniformity under inhibited conditions. The findings underscore the potential of carbon-based inhibitors in altering the corrosion morphology by reducing surface roughness and mitigating acid-induced topographical degradation.

3.5.3 Water contact angle measurement. WCA measurements were employed to evaluate changes in the surface wettability of MS in acidic media, as illustrated in Fig. 12g–i. The freshly polished MS exhibited a relatively high contact angle of 72.12° , indicating a moderately hydrophobic surface (Fig. 12g). Upon immersion in the uninhibited (blank) acidic solution, the contact angle significantly decreased to 53.97° , reflecting enhanced surface hydrophilicity due to corrosion-induced roughening and surface degradation (Fig. 12h).⁷³ In



contrast, the presence of the inhibitor MK800 at a concentration of 800 ppm resulted in a notable increase in contact angle to 64.17°, suggesting a reduction in surface wettability (Fig. 12i). This improvement in hydrophobic character is attributed to the physical adsorption of MK800 molecules and the formation of a protective surface film. Although the contact angles remain below 90°, indicating that the surfaces are not fully hydrophobic, the increase observed with MK800 implies a less hydrophilic interface compared to the uninhibited condition. These observations affirm the ability of MK800 to form a passive layer on the MS surface, thereby enhancing corrosion resistance through reduced wettability and effective surface coverage.

4 Plausible corrosion inhibition mechanism

It is well established that, MS surfaces acquire a net positive charge when exposed to hydrochloric acid, primarily due to iron dissolution *via* the anodic reaction (eqn (12)) and the adsorption of hydronium ions on the metal surface, where they react with electrons to evolve hydrogen gas through the cathodic reaction (eqn (13)).⁴¹



In this environment, the inhibitor molecules anchor to the metal surface by replacing the initially adsorbed water molecules through intermolecular forces such as electrostatic attraction and van der Waals interactions.⁷⁴ Carbon nanoparticles, which possess graphitic character with partially delocalized π -electrons, exhibit strong noncovalent interactions with the positively charged MS surface *via* electrostatic physisorption (Fig. 13). These interactions are stabilized through

metal- π interactions, whereby the vacant d-orbitals of surface iron atoms ($\text{Fe}_{\text{surf}}^{2+}$) interact with the π -electron clouds of aromatic domains in the nanoparticles, a well-characterized electrostatic phenomenon.⁷⁵ Additionally, π - π stacking among adjacent CNS enhances film cohesion and surface coverage, reducing the accessibility of the corrosive electrolyte to the underlying metal.⁷⁶ The formation of an adsorbed inhibitor layer effectively suppresses further iron dissolution and concurrently retards the cathodic hydrogen evolution reaction,⁷⁷ confirming the mixed-type nature of the inhibition mechanism (eqn (14)).



Furthermore, the surfaces of carbon nanoparticles often bear loosely bound hydroxyl ($-\text{OH}$) groups, as evidenced by XPS. In acidic media, these groups undergo protonation, leading to hydronium ion formation and desorption from the carbon surface. This dehydroxylation process results in reduced surface polarity and increased hydrophobicity, enhancing the formation of a compact, water-resistant film barrier, as previously confirmed by WCA measurements.⁷⁸ The dehydroxylated surface also promotes stronger π - π stacking, more stable van der Waals interactions, and improved metal- π binding with the MS substrate. These synergistic effects result in enhanced surface coverage (θ) and effective physisorption, which are corroborated by EIS through decreased double-layer capacitance (C_{dl}) and increased charge-transfer resistance (R_p).⁴⁵ Since both the anodic and cathodic reactions are suppressed, MK800 may be classified as a mixed-type inhibitor, as evidenced by PDP and EIS measurements. Collectively, these phenomena translate into lower electron exchange rates and reduced corrosion activity.

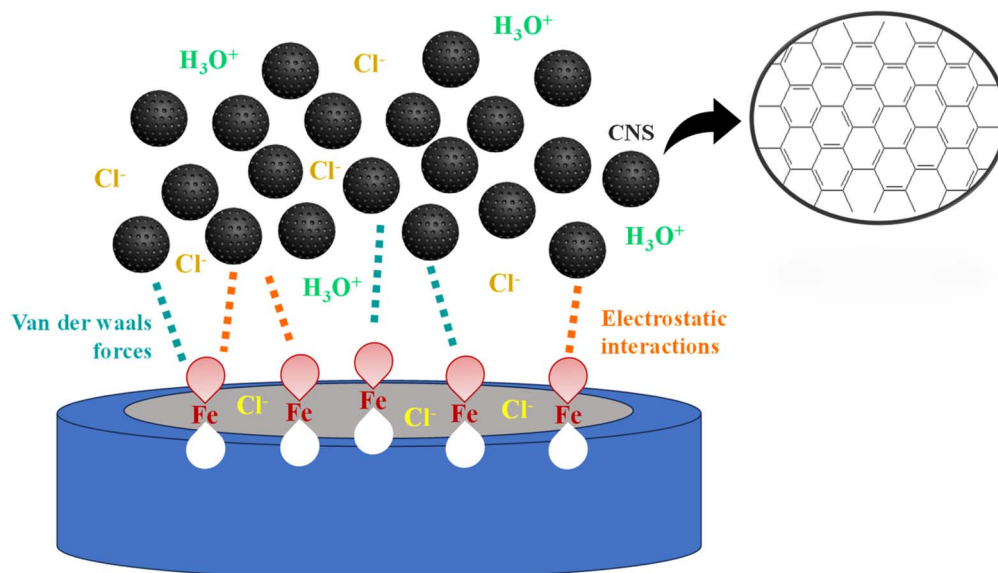


Fig. 13 Proposed corrosion inhibition mechanism of MK800.



5 Conclusions

The present study demonstrates that MK800 is an effective corrosion inhibitor for mild steel in 1 M HCl solution. The synthesis of MK800 was confirmed through FE-SEM, TEM, XRD, XPS, and BET analyses, which collectively verified the formation of porous, spherical graphitic carbon nanostructures. Electrochemical investigations revealed that MK800 exhibits mixed-type inhibition characteristics, significantly suppressing both anodic and cathodic processes. The inhibition efficiency was found to increase with both inhibitor concentration and temperature. Electrochemical impedance spectroscopy confirmed the formation of a protective inhibitor layer through increased polarization resistance and decreased double-layer capacitance. Adsorption studies indicated that MK800 adheres to the mild steel surface *via* a Langmuir adsorption isotherm, suggesting monolayer coverage and predominantly physical adsorption (-16.084 to -17.696 kJ mol⁻¹). Surface characterization techniques, including SEM, EDS, optical profilometry, and contact angle measurements, further substantiated the presence of an adsorbed protective film, confirming the surface-active nature of the inhibitor. Collectively, the findings establish MK800 as a promising corrosion mitigation agent for mild steel in acidic environments (HCl), with its inhibition efficiency governed by adsorption-driven surface passivation.

Author contributions

Anvitha Murari: conceptualization, methodology, analysis, investigation and writing – Original draft preparation. Arathi A: data curation, analysis and editing. Uraivan Sirimahachai: visualization, investigation. Srilatha Rao: writing – reviewing and editing. Gurumurthy Hegde: supervision, writing – reviewing and editing.

Conflicts of interest

There are no conflicts to declare.

Data availability

Data is available with the relevant request to the authors.

Supplementary information (SI) is available. See DOI: <https://doi.org/10.1039/d5ra09725h>.

Acknowledgements

One of the authors, AM, likes to acknowledge Central Instrumentation Facility, Christ University for providing FESEM, Raman and XRD facilities.

References

- B. S. Mahdi, M. K. Abbass, M. K. Mohsin, W. K. Al-Azzawi, M. M. Hanoon, M. H. H. Al-Kaabi, L. M. Shaker, A. A. Al-Amiery, W. N. R. W. Isahak, A. A. H. Kadhum and M. S. Takriff, *Molecules*, 2022, **27**, 4857.
- H. Rahal, A. M. Abdel-Gaber, M. S. El-Rifai and S. El-Housseiny, *Mor. J. Chem.*, 2024, **12**, 1554–1574.
- F. Ennafaa, A. Chraka, K. Tassaoui, I. Mouamr, M. Damej, A. E. L. Mahmoudi, K. Bougrin, H. T. Rahal and M. Benmessaoud, *Mater. Chem. Phys.*, 2025, **334**, 130441.
- L. W. El Khatib, H. T. Rahal and A. M. Abdel-Gaber, *Prot. Met. Phys. Chem. Surf.*, 2020, **56**, 1096–1106.
- M. López Freixes, L. Peguet, T. Warner and B. Gault, *Corros. Sci.*, 2024, **229**, 111904.
- M. Wu, T. Wang, K. Wu and L. Kan, *Constr. Build. Mater.*, 2020, **239**, 117813.
- J. K. Emmanuel, *Bull. Natl. Res. Cent.*, 2024, **48**, 26.
- D. H. Abdeen, M. El Hachach, M. Koc and M. A. Atieh, *Materials (Basel)*, 2019, **12**, 210.
- J. Liu, N. Wang, F. Zheng, C. Wang, J. Wang, B. Hou, Q. Zhao, Y. Ning and Y. Hu, *J. Mater. Sci. Technol.*, 2022, **122**, 211–218.
- A. Kadhim, A. A. Al-Amiery, R. Alazawi, M. K. S. Al-Ghezi and R. H. Abass, *Int. J. Corros. Scale Inhib.*, 2021, **10**, 54–67.
- S. Km, B. M. Praveen and B. K. Devendra, *Results in Surfaces and Interfaces*, 2024, **16**, 100258.
- A. Ashwathareddy, S. Rao, S. Shree Subramaniyam, P. Gopala Krishna, K. Monnppa Rama and S. Kodange, *Inorg. Chem. Commun.*, 2024, **169**, 113071.
- A. A. Al-Amiery, W. N. R. W. Isahak and W. K. Al-Azzawi, *Lubricants*, 2023, **11**, 174.
- A. Veeramanocharan and S.-C. Kim, *RSC Adv.*, 2024, **14**, 25429–25471.
- P. B. Raja and M. G. Sethuraman, *Mater. Lett.*, 2008, **62**, 113–116.
- J. S. Câmara, R. Perestrelo, R. Ferreira, C. V. Berenguer, J. A. M. Pereira and P. C. Castilho, *Molecules*, 2024, **29**, 3861.
- C. Pan, J. He, J. Zhu, S. Li, W. Li, W. Yang and W. Li, *ACS Appl. Nano Mater.*, 2024, **7**, 2515–2528.
- D. S. Chauhan, M. A. Quraishi, K. R. Ansari and T. A. Saleh, *Prog. Org. Coat.*, 2020, **147**, 105741.
- L.-C. Jing, W.-H. Geng, Z.-L. Bao, P.-F. Qian, R.-Y. Chang, T.-Y. Li, Y.-L. Guo, D. Zhang and H.-Z. Geng, *J. Colloid Interface Sci.*, 2025, **680**, 479–495.
- Z. Shirazi, A. N. Golikand and M. H. Keshavarz, *J. Iran. Chem. Soc.*, 2024, **21**, 409–419.
- D. Zhen, S. Zhang, X. Zhang, H. Zhang, J. Wang, B. Chen, Y. Liu and X. Luo, *Int. J. Biol. Macromol.*, 2023, **253**, 126449.
- G. K. Kuriya, V. M. Paiva, S. M. de Oliveira, A. C. Teixeira, C. M. da S. de Almeida, J. E. L. Mateus, J. R. de Araujo, M. E. H. Maia da Costa, N. M. Suguihiro and E. D'Elia, *ACS Omega*, 2025, **10**, 33253–33269.
- M. Goyal, S. Sanyukta and S. Kumar, in *Nanoscience & Nanotechnology Series*, Royal Society of Chemistry, Cambridge, 2022, pp. 63–76.
- Z. Wang, D. Shen, C. Wu and S. Gu, *Green Chem.*, 2018, **20**, 5031–5057.
- P. W. Mwaurah, S. Kumar, N. Kumar, A. Panghal, A. K. Attkan, V. K. Singh and M. K. Garg, *Compr. Rev. Food Sci. Food Saf.*, 2020, **19**, 2421–2446.
- S. Punia Bangar, M. Kumar and W. S. Whiteside, *Int. J. Biol. Macromol.*, 2021, **183**, 1807–1817.



- 27 T. Tesfaye, J. K. Johakimu, R. B. Chavan, B. Sithole and D. Ramjugernath, *Clean Technol. Environ. Policy*, 2018, **20**, 81–94.
- 28 P. S. Awodi, J. C. Ogbonna and T. N. Nwagu, *Heliyon*, 2022, **8**, e09707.
- 29 V. Molahalli, V. S. Bhat, A. Sharma, G. Soman and G. Hegde, *RSC Adv.*, 2025, **15**, 14183–14193.
- 30 G. Soman, K. Sayeed, K. Pandey, U. Sirimahachai and G. Hegde, *J. Energy Storage*, 2025, **121**, 116590.
- 31 B. Sirichandana, R. Silviya, S. V. Bhat, N. Patel and G. Hegde, *Nanoscale Adv*, 2025, **7**, 4056–4066.
- 32 M. S. Khosrowshahi, M. A. Abdol, H. Mashhadimoslem, E. Khakpour, H. B. M. Emrooz, S. Sadeghzadeh and A. Ghaemi, *Sci. Rep.*, 2022, **12**, 8917.
- 33 M. Kim, H. Lim, X. Xu, M. S. A. Hossain, J. Na, N. N. Awaludin, J. Shah, L. K. Shrestha, K. Ariga, A. K. Nanjundan, D. J. Martin, J. G. Shapter and Y. Yamauchi, *Microporous Mesoporous Mater.*, 2021, **312**, 110757.
- 34 B. G. M. Patel, S. S. Islam, S. Mandal, S. Bose and G. Hegde, *J. Environ. Chem. Eng.*, 2025, **13**, 115879.
- 35 F. Bentiss, M. Traisnel and M. Lagrenee, *Corros. Sci.*, 2000, **42**, 127–146.
- 36 M. Behpour, S. M. Ghoreishi, N. Soltani, M. Salavati-Niasari, M. Hamadani and A. Gandomi, *Corros. Sci.*, 2008, **50**, 2172–2181.
- 37 X.-F. Wang, X.-Y. Liu, F. Su, J.-S. Li, Z.-M. Zhu, X.-J. Sang and L.-C. Zhang, *ACS Omega*, 2022, **7**, 4429–4443.
- 38 M. Gouda and H. M. A. El-Lateef, *Molecules*, 2021, **26**, 7006.
- 39 S. Kumari, N. Sandhu, V. Saraswat and T. K. Sarkar, *Langmuir*, 2025, **41**, 12150–12165.
- 40 P. H. Renuka, S. Rao, P. Rao, S. Shree S and G. K. Prashanth, *Inorg. Chem. Commun.*, 2024, **160**, 111871.
- 41 T. D. Manh, T. L. Huynh, B. V. Thi, S. Lee, J. Yi and N. Nguyen Dang, *ACS Omega*, 2022, **7**, 8874–8886.
- 42 V. Choudhary, S. Dua, N. Arora, R. C. Saxena, B. G. Prakashaiah, T. Senthilkumar, M. M. Singh, T. S. Khan and S. K. Ganguly, *Discov. Chem.*, 2025, **1**, 100112.
- 43 A. Zaher, H. Lgaz, A. Boukhraz, A. Aldalbahi, H.-S. Lee, B. Bourkhiss and M. Ouhssine, *Coatings*, 2024, **14**, 1556.
- 44 L. Chen, D. Lu and Y. Zhang, *Materials (Basel)*, 2022, **15**, 2023.
- 45 S. Zehra, R. Aslam and M. Mobin, in *Recent Developments in Analytical Techniques for Corrosion Research*, Springer International Publishing, Cham, 2022, pp. 91–117.
- 46 V. D. Jović, *Mater.*, 2022, **63**, 50–57.
- 47 Y. Li, D. Wang and L. Zhang, *RSC Adv.*, 2019, **9**, 26464–26475.
- 48 A. Thakur, S. Kaya, A. S. Abousalem and A. Kumar, *Sustain. Chem. Pharm.*, 2022, **29**, 100785.
- 49 M. M. Solomon and S. A. Umoren, *J. Adhes. Sci. Technol.*, 2015, **29**, 2311–2333.
- 50 S. Yahya, N. K. Othman, A. R. Daud, A. Jalar and R. Ismail, *Anti-Corros. Methods Mater*, 2015, **62**, 301–306.
- 51 R. Aslam, M. Mobin, M. Shoeb and J. Aslam, *Sci. Rep.*, 2022, **12**, 9274.
- 52 H. M. El Refay, A. M. Hyba and G. A. Gaber, *Chem. Pap.*, 2022, **76**, 813–825.
- 53 H. Kumar, Rajrani, R. Sharma, A. Yadav and R. Kumari, *Chem. Data Coll.*, 2020, **29**, 100527.
- 54 L.-C. Jing, W.-H. Geng, Z.-L. Bao, P.-F. Qian, R.-Y. Chang, T.-Y. Li, Y.-L. Guo, D. Zhang and H.-Z. Geng, *J. Colloid Interface Sci.*, 2025, **680**, 479–495.
- 55 D. Zhen, S. Zhang, X. Zhang, H. Zhang, J. Wang, B. Chen, Y. Liu and X. Luo, *Int. J. Biol. Macromol.*, 2023, **253**, 126449.
- 56 Y. Ye, D. Yang, H. Chen, S. Guo, Q. Yang, L. Chen, H. Zhao and L. Wang, *J. Hazard. Mater.*, 2020, **381**, 121019.
- 57 L. Dong, Y. Ma, X. Jin, L. Feng, H. Zhu, Z. Hu and X. Ma, *ACS Omega*, 2023, **8**, 46934–46945.
- 58 B. A. Abd-El-Nabey, M. E. Mahmoud, A. Abdelrahman Saad and M. A. Abd-El-Fatah, *Corros. Eng. Sci. Technol.*, 2025, DOI: [10.1177/1478422x251398913](https://doi.org/10.1177/1478422x251398913).
- 59 O. J. Oluwole, D. N. Anyiam, Y. D. Balogun, O. P. Oluwole and I. E. Awomade, *Int. J. Recent Res. Soc. Sci. Humanit.*, 2024, **11**, 115–124.
- 60 N. Timoudan, A. S. Al-Gorair, L. El Foujji, I. Warad, Z. Safi, B. Dikici, F. Benhiba, A. E. K. Qaiss, R. Bouhfid, F. Bentiss, S. S. Al-Juaid, M. Abdallah and A. Zarrouk, *RSC Adv.*, 2024, **14**, 30295–30316.
- 61 A. M. Ashmawy, A. M. El-Sawy and H. F. Khalil, *Mol. Cryst. Liq. Cryst.*, 2022, **736**, 9–29.
- 62 I. Ahamad, R. Prasad and M. A. Quraishi, *Corros. Sci.*, 2010, **52**, 933–942.
- 63 L. T. Popoola, *Corros. Rev.*, 2019, **37**, 71–102.
- 64 J. I. Bhat and V. D. P. Alva, *Int. J. Electrochem.*, 2011, **2011**, 1–8.
- 65 P. O. Ameh and P. c. Ukoha, *Ind. Chem.*, 2017, **3**, 1000119.
- 66 A. Fawzy, R. El-Sayed, A. Al Bahir, M. Morad, I. Althagafi and K. Althagafy, *J. Adhes. Sci. Technol.*, 2022, **36**, 1993–2019.
- 67 Y. Aoufir, Y. Bakri, A. Chaouiki, H. Lgaz, H. Oudda, R. Salghi, A. Guenbour and E. M. Essassi, *Port. Electrochim. Acta*, 2021, **39**, 105–133.
- 68 A. I. Ikeuba, J. E. Ntibi, P. C. Okafor, B. I. Ita, A. U. Agobi, F. C. Asogwa, B. J. Omang, E. A. Eno, H. Loius, S. A. Adalikwu, B. A. Abiola, F. E. Abeng and N. A. Abang, *Results Chem.*, 2023, **5**, 100909.
- 69 M. Azadi, M. Mehrabadi and A. Hafazeh, *Results Eng.*, 2025, **26**, 105147.
- 70 H. M. El Refay, A. M. Hyba and G. A. Gaber, *Chem. Pap.*, 2022, **76**, 813–825.
- 71 R. K. Mehta, S. K. Gupta and M. Yadav, *Diam. Relat. Mater.*, 2023, **136**, 109992.
- 72 P. M. Krishnegowda, V. T. Venkatarangaiah, P. K. M. Krishnegowda, A. N. Subba Rao and S. H. Nataraj, *J. Electrochem. Sci. Eng.*, 2024, **14**, 279.
- 73 M. Mobin, Huda, S. Zamindar and P. Banerjee, *J. Mol. Liq.*, 2023, **385**, 122403.
- 74 R. J. Maurer, V. G. Ruiz, J. Camarillo-Cisneros, W. Liu, N. Ferri, K. Reuter and A. Tkatchenko, *Prog. Surf. Sci.*, 2016, **91**, 72–100.
- 75 C. Verma, M. A. Quraishi, E. E. Ebenso and C. M. Hussain, *Nano Sel*, 2021, **2**, 2237–2255.
- 76 J. C. Ma and D. A. Dougherty, *Chem. Rev.*, 1997, **97**, 1303–1324.
- 77 S. G. Croll, *Prog. Org. Coat.*, 2020, **148**, 105847.
- 78 T. Szabó, E. Tombácz, E. Illés and I. Dékány, *Carbon N. Y.*, 2006, **44**, 537–545.

